Nitrogen-doped carbon nanotubes coated by atomic layer deposited SnO$_2$ with controlled morphology and phase

Xiangbo Meng, Yu Zhong, Yifan Sun, Mohammad Norouzi Banis, Ruying Li, Xueliang Sun *

Department of Mechanical and Materials Engineering, The University of Western Ontario, London, ON, Canada N6A 5B9

ARTICLE INFO

ABSTRACT

Atomic layer deposition (ALD) was used to synthesize metal oxide-carbon nanotube (MO-CNT) hybrid materials by coating nitrogen-doped CNTs (N-CNTs). SnO$_2$-CNT hybrids were produced using SnCl$_4$ and water as precursors and exhibited many unique features. It was demonstrated that the use of N-CNTs was beneficial for directly initiating the ALD of SnO$_2$ (ALD-SnO$_2$) and that adjustable ALD parameters were favorable for controlling the morphology and phase of the deposited SnO$_2$. The cyclic and surface-controlled nature of ALD contributed to the morphologies of SnO$_2$ tunable from nanoparticles to nanofilms, and the temperature-dependent characteristics of the ALD-SnO$_2$ rendered the phases of SnO$_2$ controllable with amorphous, crystalline, or a mixed phase by the former two. Furthermore, this study also explored the underlying mechanisms for the controlled synthesis of SnO$_2$-CNT hybrid materials.

1. Introduction

There was a long history for the discoveries of carbon nanotubes (CNTs) [1], but only after Iijima's work [2] was an extensive investigation boosted with many findings on their exceptional properties and significant applications [3]. A primary approach for applications was to incorporate CNTs with other materials, and the resultant hybrid materials in general exhibited improved properties. Of them, CNT-based metal oxide (MO-CNT) hybrids represent an important class and are very promising as functional materials, such as in lithium-ion batteries (LIBs) and supercapacitors [4].

Tin (IV) dioxide (SnO$_2$) is among the most investigated nanoscale MOs, ascribing to its distinctive properties very useful in many areas (e.g., field emission [5,6], gas sensors [7], and LIBs [8–10]). In comparison, CNT-based SnO$_2$ (SnO$_2$-CNT) hybrids are much superior to their pure SnO$_2$ tubular counterparts, e.g., exhibiting higher sensitivity as gas sensors [11,12], as well as increased specific mass capacity and extended durability as anodes of LIBs [13–20]. Thus, a large amount of effort has previously devoted to develop SnO$_2$-CNT hybrids using various methods including arc-discharge [13], chemical vapor deposition (CVD) [14], and different chemical-solution routes [15–20]. However, the used CNTs required a pretreatment process to modify their inert surface nature before a deposition of SnO$_2$ was performed. This could be realized either by acid oxidation [14–19] or by surfactants [20]. Unfavorably, the two functionalization methodologies of CNTs commonly needed wet chemical treatment, while the former one further risked CNTs to some damages in their inherent properties. As a consequence, the previous methods [13–20] were confined with a limited flexibility and they exclusively produced polycrystalline nanoparticles of SnO$_2$ on functionalized CNTs.

To bypass the drawbacks suffered by earlier studies, we recently developed an alternative strategy to synthesize MO-CNT hybrids, in which the technique of atomic layer deposition (ALD) was used to coat nitrogen-doped CNTs (N-CNTs) directly. As a consequence, it was demonstrated that the ALD route as well as the use of N-CNTs brought many unique

advantages. First of all, N-CNTs by nature are chemically active [21] and thereby can directly induce the following ALD of SnO_2 (ALD-SnO_2). Furthermore, ALD is a surface-controlled and layer-by-layer process, relying on two sequential self-terminating half-reactions [22–24]. Thus, ALD is superior in deposition with high flexibility and preciseness. As for ALD-SnO_2, some earlier efforts practiced the deposition on flat substrates and nanoparticles using different precursors [25–35]. However, there were no cases to date reported on the ALD-SnO_2 on CNTs. In this study, we attempted to achieve this goal using N-CNTs as substrates, as well as $SnCl_4$ and water as precursors. In essence, the reaction between $SnCl_4$ and H_2O is fairly straightforward with the product of SnO_2, as described in the following reaction:

$$SnCl_4 + 2H_2O \rightarrow SnO_2 + 4HCl \qquad (1)$$

In ALD-SnO_2, the above reaction was previously interpreted by two half-reactions [33]:

$$\|-OH + SnCl_4(g) \rightarrow \|-OSnCl_3 + HCl(g) \qquad (2\text{-A})$$
$$\|-Cl + H_2O(g) \rightarrow \|-OH + HCl(g) \qquad (2\text{-B})$$
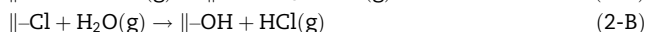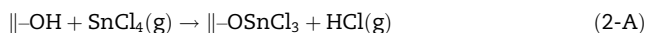
where "$\|$" indicates the substrate surface, and "(g)" denotes the vapor species. With the fulfillment of ALD-SnO_2 on N-CNTs, it was found in this study that the deposited SnO_2 is controllable in morphology as well as structural phase. In particular, it was also revealed that the ALD-SnO_2 is highly temperature-dependent. Thus, besides the aforementioned two half-reactions, other underlying mechanisms for ALD-SnO_2 were developed as well. In summary, there are three features induced by the proposed strategy (i.e., ALD-SnO_2 on N-CNTs): (i) the N-CNTs are free of external functionalization; (ii) the deposited SnO_2 materials are tunable in morphology from nanoparticles to nanofilms; (iii) the deposited SnO_2 materials are controllable in structural phase from amorphous to crystalline or a mixed phase by the former two. Thus, this work opened an avenue for highly precise synthesis of CNT-based hybrids and provided multiple candidates for many important applications, such as gas sensors, and LIBs.

2. Experimental

2.1. Synthesis of N-CNTs

A thermal CVD method was applied to grow N-CNTs on substrates (carbon papers or Si wafers). The substrates were initially coated with a buffer layer of 30 nm thick aluminum and a catalyst layer of 5 nm thick iron. In the presence of Ar, the pyrolysis of melamine ($C_3H_6N_6$) at 800 °C induced the growth of N-CNTs on the substrates. The synthesized N-CNTs were structurally multi-walled and bamboo-like, presenting a typical N content of over 10 at.%. More details were described in a previous work [36].

2.2. ALD-SnO_2

ALD-SnO_2 was performed on the synthesized N-CNTs through supplying tin (IV) chloride (99% $SnCl_4$, Sigma–Aldrich) and deionized water into a commercial ALD reactor (Savannah 100, Cambridge Nanotechnology Inc., USA) in an alternating manner. The temperature of the ALD reactor was in a range 200–400 °C. Nitrogen was used as the carrier gas with a flow rate of 20 sccm, and the ALD reactor was sustained at a low level of base pressure (typically 0.4 Torr) by a vacuum pump (Pascal 2005 I, Adixon). The ALD procedures were set as follows: (1) a 0.5 s supply of $SnCl_4$; (2) a 3 s extended exposure of $SnCl_4$ to N-CNTs; (3) a 10 s purge of oversupplied $SnCl_4$ and any by-products; (4) a 1 s supply of water vapor; (5) a 3 s extended exposure of water to N-CNTs; (6) a 10 s purge of oversupplied water and any by-products. The aforementioned six-step sequence constituted one ALD-SnO_2 cycle and the ALD processes could differ in the number of cycles.

2.3. Characterization

The synthesized N-CNTs and SnO_2-CNT hybrid materials were characterized using a field-emission scanning electron microscope (FE-SEM, Hitachi 4800S) equipped with energy dispersive X-ray spectroscopy (EDS), transmission electron microscope (TEM, Philips CM10), high-resolution TEM (HRTEM, JEOL 2010 FEG), micro X-ray diffractometer (XRD, Brucker D8, Cu Kα radiation, λ = 1.5406 Å), and X-ray photoelectron spectrometer (XPS, Kratos Axis Ultra Al K(alpha)).

3. Results and discussion

3.1. Results

In Fig. 1(a) and (b), the synthesized N-CNTs are shown by SEM images of low and high magnification, respectively. Fig. 1(a) reveals that the N-NCTs were grown on carbon papers with high density, and Fig. 1(b) shows that they are morphologically bamboo-like with diameters in the range 40–80 nm. Fig. 1(c) presents the XRD spectra of two samples coated by ALD-SnO_2 at 200 and 400 °C. The two samples commonly exhibit two strong peaks at 26.38° and 54.54°, consistent with those reference values of crystalline graphite (JCPDS PDF No. 41-1487). The two peaks are apparently induced by pristine N-CNTs and marked as Graphite(0 0 2) and Graphite(0 0 4), respectively. To further identify the information of SnO_2, the XRD spectra between 30° and 55° are magnified in the inset of Fig. 1(c). It is found that the sample coated at 400 °C (marked with a solid square) presents several characteristic peaks of crystalline SnO_2 (JCPDS PDF No. 41-1445) at 33.89°, 42.63°, and 51.78°, corresponding to the (1 0 1), (2 1 0), and (2 1 1) plane, respectively. Another sample coated at 200 °C (marked with a solid triangle) has no observable peaks in the range 30–55°, implying an amorphous state of the deposited SnO_2. Furthermore, EDS spectra in Fig. 1(d) confirm the presence of Sn and O element with the sample coated at 200 °C. As for other elements, C is attributed to N-CNTs, both Al and Fe are from the coatings of carbon papers, and Cl is due to some remaining Cl ligands. Thus, it is reasonable to conclude that growth temperatures are determinant for the phases of the deposited SnO_2.

To further characterize the synthesized SnO_2-CNT hybrid materials, we applied SEM, TEM, and HRTEM. Fig. 2 shows the SnO_2-CNT hybrids synthesized at 200 °C. SEM images of Fig. 2(a), (c), and (e) correspond to the ALD-SnO_2 of 50, 100, and 200 cycles, respectively. They commonly reveal that, in
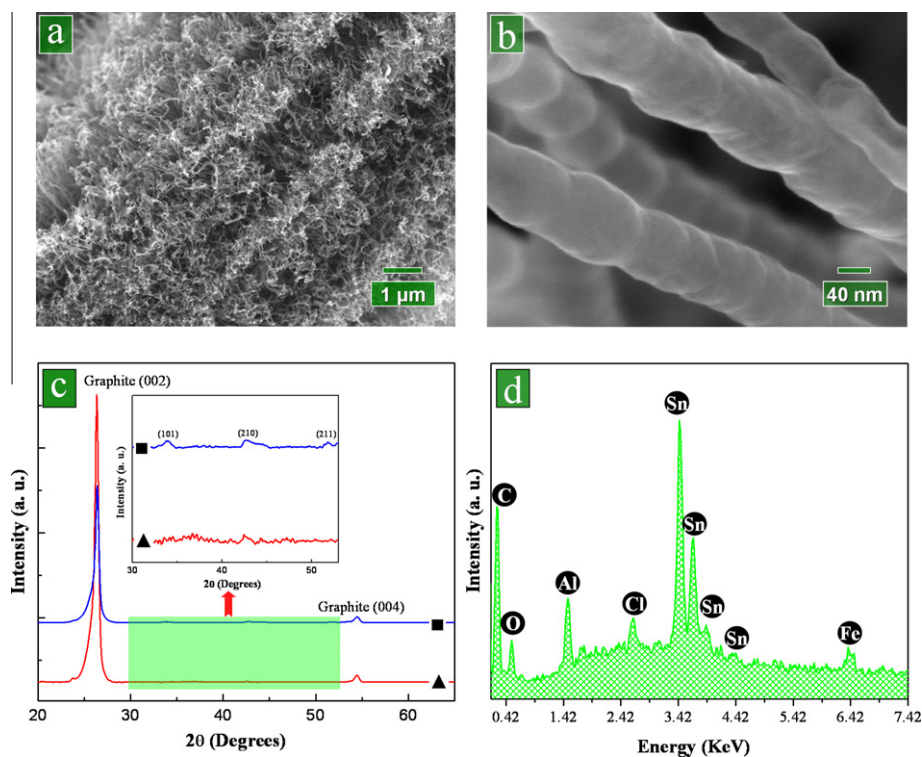
Fig. 1 – SEM images of N-CNTs with (a) low magnification, and (b) high magnification; (c) XRD spectra of N-CNTs coated with 200-cycle ALD-SnO$_2$ at (▲) 200 °C and (■) 400 °C; (d) EDS spectra of N-CNTs coated with 200-cycle ALD-SnO$_2$ at 200 °C.

comparison to pristine N-CNTs illustrated in Fig. 1(b), the surface of N-CNTs becomes rougher with a coating of some external material. According to Reactions (2-A) and (2-B), the material deposited externally should be SnO$_2$ and the information from Fig. 1(c) and (d) discloses the deposited SnO$_2$ in an amorphous state. Furthermore, the corresponding TEM images in Fig. 2(b), (d), and (f) jointly reveal that the morphological evolution of SnO$_2$ experienced three stages: separated nanoparticles (3–5 nm, Fig. 2(b)), coalescence of nanoparticles (Fig. 2(d)), and formation of a coaxial nanofilm (Fig. 2(f)). In particular, the patterns of selected area electron diffraction (SAED, inset of Fig. 2(f)) show the disordered nature of the hybrid material, which confirms the amorphous nature of the deposited SnO$_2$. Additionally, the case of 200-cycle ALD-SnO$_2$ was further analyzed by HRTEM, as shown in Fig. 2(g) and (h). Fig. 2(g) shows that, besides the graphene layers of N-CNTs, there is no crystalline structure with the deposited SnO$_2$. Fig. 2(h) also reveals the amorphous nature of the deposited SnO$_2$ and exposes a uniform film thickness of around 2.6 nm. As a consequence, the amorphous SnO$_2$ reached an average growth of around 0.13 Å/cycle at the temperature of 200 °C.

Following up the synthesis of SnO$_2$-CNT hybrid materials at 200 °C, a high temperature of 400 °C was applied to continue the synthesis and the main results are included in Fig. 3. As disclosed by the SEM image of Fig. 3(a), a 50-cycle ALD-SnO$_2$ seemingly produced only nanoparticles of around 10 nm on N-CNTs. Further increasing ALD-SnO$_2$ to 100 (Fig. 3(b)), 200 (Fig. 3(c)), and 400 cycles (Fig. 3(d)) prompted

the growth of nanoparticles in size (up to 50 nm) and density but there were no films formed on N-CNTs. The TEM image (Fig. 3(e)) for the case of 100-cycle ALD-SnO$_2$ confirms that, besides nanoparticles, there were no others deposited on N-CNTs. SAED discloses a polycrystalline nature of the deposited nanoparticles, consistent to the XRD result in Fig. 1(c). The HRTEM images in Fig. 3(f) and (g) show clearly the crystalline structures of both SnO$_2$ and N-CNTs. It is noteworthy that, besides some big nanoparticles (around 20 nm) as disclosed in Fig. 3(e), a large amount of tiny nanoparticles of less than 5 nm are exposed in Fig. 3(f) and (g), as red-circled[1] in the images. In particular, it is noted that the deposited nanoparticles are predominately located in the interlinked areas of N-CNTs. Thus, it is apparent that nanoparticles did not grow with a same rate. Furthermore, as indicated in Fig. 3(f) and (g), there are two kinds of lattice planes identified with the nanoparticles. The inter-plane spacing of 0.335 nm corresponds to the (1 1 0) plane, while the one of 0.264 nm corresponds to the (1 0 1) plane of SnO$_2$. It is worth noting that the (1 1 0) plane of SnO$_2$ has not been identified in XRD spectrum (Fig. 1(c)), for its characteristic position at 26.61° is very close to that of Graphite(0 0 2).

Based on the above-disclosed results, it is evident that growth temperatures are crucial for ALD-SnO$_2$ on N-CNTs. To further investigate the effects of growth temperature, an intermediate temperature of 300 °C was used to synthesize SnO$_2$-CNT hybrids, and the resultant results are illustrated in Fig. 4. Along with the increasing ALD-SnO$_2$ from 50 (Fig. 4(a)), 100 (Fig. 4(b)) to 200 cycles (Fig. 4(c)), one can

---

[1] For interpretation of color in Figs. 3 and 8, the reader is referred to the web version of this article.
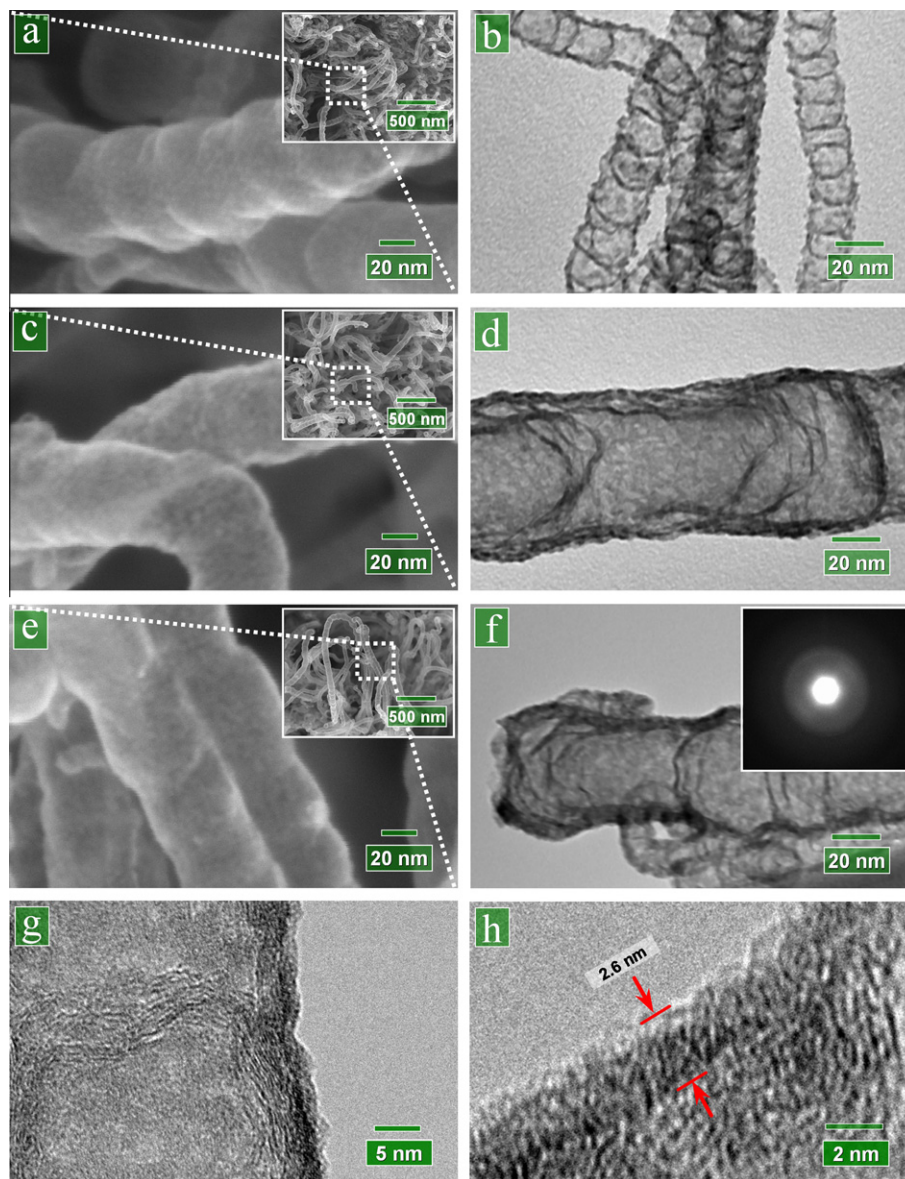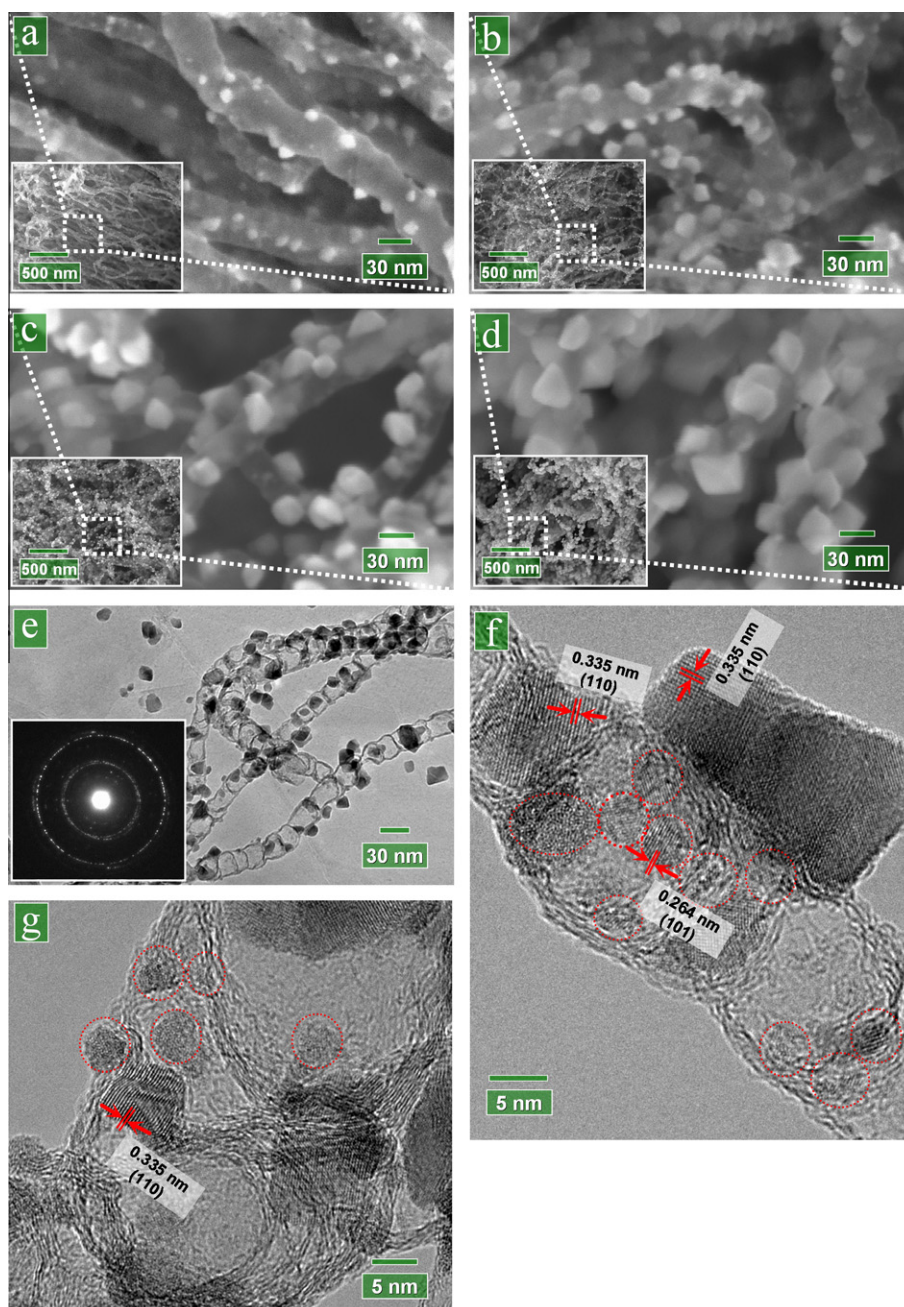
Fig. 2 – ALD-SnO$_2$ on N-CNTs at 200 °C. SEM images after (a) 50, (c) 100, and (e) 200 ALD cycles; TEM images after (b) 50, (d) 100, and (f) 200 ALD cycles (inset: SAED patterns); (g and h) HRTEM images of 200-cycle ALD-SnO$_2$.

observe numerous nanoparticles deposited on N-CNTs with increased sizes, accounting for 3–5 nm, 3–7 nm, to 5–15 nm, respectively. However, besides nanoparticles presenting white and bright spots in the images, the intervals between nanoparticles seem also covered with a continuous layer. Fig. 4(d) shows the TEM image for the case of 200-cycle ALD-SnO$_2$, and the corresponding SAED patterns in the inset of Fig. 4(d) disclose that the deposited SnO$_2$ presents polycrystalline characteristics. Under the HRTEM examination (Fig. 4(e) and (f)), it is worth noting that a 2.6 nm thick amorphous nanofilm and many crystalline nanoparticles are observed. The nanoparticles show clearly an inter-plane of 0.335 nm, corresponding to the (1 1 0) plane of SnO$_2$. Obviously, the crystalline nanoparticles are responsible for the polycrystalline nature of the SAED patterns (the inset of Fig. 4(d)). Thus, an intermediate growth temperature prompted a covering of heterogeneous structural phases,

i.e., an amorphous film embellished with crystalline nanoparticles.

Upon this point, it was clearly demonstrated that the proposed strategy shows a strong capability in synthesizing SnO$_2$-CNT hybrids as well as in controlling the deposited SnO$_2$ with different phases and morphologies. To summarize, there are three main features exhibited by the synthesized SnO$_2$-CNTs hybrids: (i) direct initiation of ALD-SnO$_2$ on N-CNTs; (ii) controllable phases of the deposited SnO$_2$ with temperature, showing amorphous (Fig. 2), crystalline (Fig. 3), or even a mixed amorphous-crystalline phase (Fig. 4); (iii) tunable morphologies of the deposited SnO$_2$, exhibiting nanoparticles (Figs. 2 and 3), nanofilms (Fig. 2), or a mixture of nanofilms and nanoparticles (Fig. 4). To understand these interesting results, it is believed that both the effects of N-CNTs and the underlying mechanisms of ALD-SnO$_2$ are essential. In particular, their distinctive dependence on

Fig. 3 – ALD-SnO$_2$ on N-CNTs at 400 °C. SEM images after (a) 50, (b) 100, (c) 200, (d) 400 ALD cycles; (e) TEM image of 100-cycle ALD-SnO$_2$ (inset: SAED patterns); (f and g) HRTEM images of 100-cycle ALD-SnO$_2$.

temperature should be clarified. Thus, we investigated them and will discuss in the following sections.

3.2. Discussion

3.2.1. The effects of N-doping

As stated above, one feature with this study is the use of N-CNTs which initiated ALD-SnO$_2$ directly. As a surface-controlled process, ALD initiates on a substrate via an interaction between the molecules of one precursor and the reactive sites of the substrate. This kind of interaction contributes to an irreversible adsorption of one precursor and is restricted to chemisorption [37]. In comparison to pure (undoped) CNTs

used in previous studies [14–20], the difference of N-CNTs lies in their N-doping. Therefore, the N-doping is responsible for the reactivity of N-CNTs and thereby for the initiation of ALD-SnO$_2$. In this case, an investigation on the effects of N-doping is crucial for a better understanding of the ALD-SnO$_2$ on N-CNTs.

Of the two precursors (SnCl$_4$ and H$_2$O) used in this study, H$_2$O could only be possible to physically adsorb on the N-CNTs and the adsorption of these molecules can be reversed easily [38]. In this case, SnCl$_4$ holds as the only candidate to chemically bond with N-related defective sites and to initiate the ALD-SnO$_2$ on N-CNTs. Evidence from earlier studies [39–41] demonstrated that metal atoms could bond with N-related
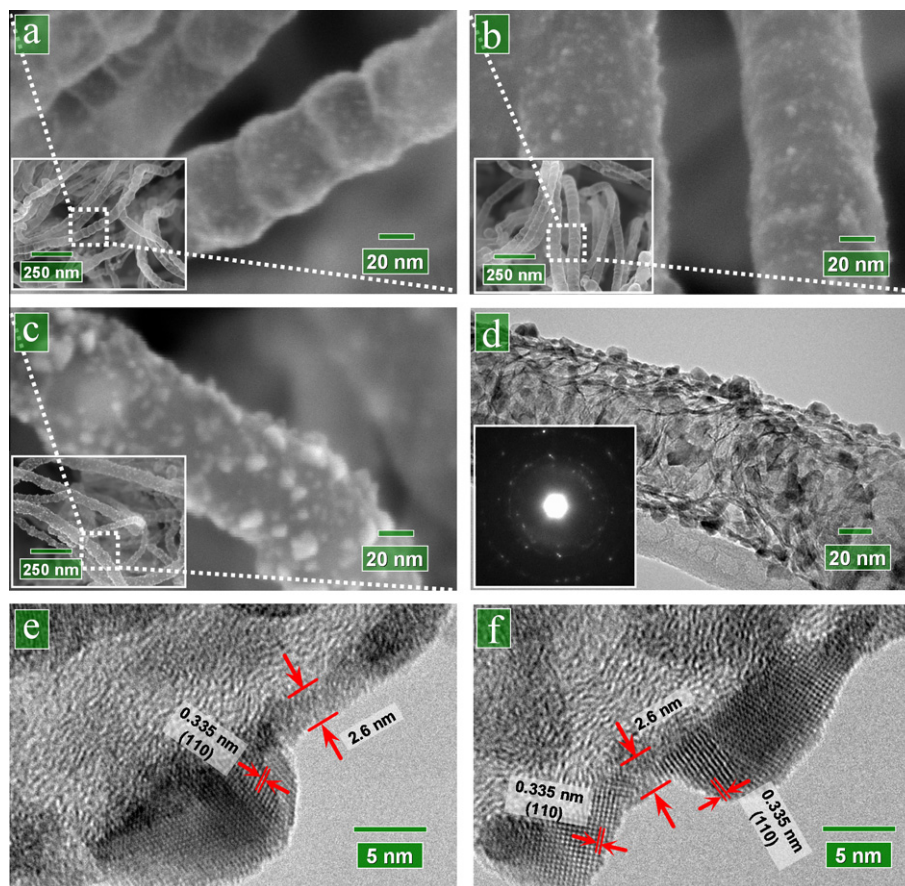
Fig. 4 – ALD-SnO$_2$ on N-CNTs at 300 °C. SEM images after (a) 50, (b) 100, and (c) 200 ALD cycles; (d) TEM image of 200-cycle ALD-SnO2 (inset: SAED patterns); (e and f) HRTEM images of 200-cycle ALD-SnO$_2$.

defective sites and thereby induce the growth of metal nanoparticles or nanowires on N-CNTs. In addition, they also disclosed that the effects of N-doping are closely related with the doped-N configurations, for different doped-N configurations have distinctive mechanisms to adsorb metal atoms. Thus, it would be better to investigate the effects of N-doping according to their configurations. As for the configurations of the doped-N atoms, there are several ones identified to date, including gaseous N$_2$, nitric oxides, pyridine-like nitrogen, graphite-like nitrogen, and pyrrolic nitrogen [42,43]. Although these doped-N configurations might not appear concurrently [44], there are two primary ones commonly exposed in N-CNTs, i.e., graphite-like (in which a nitrogen atom replaces a graphitic carbon atom) and pyridine-like N configuration (in which a nitrogen atom bonds with two carbon atoms). Furthermore, it was also experimentally [39–41] and theoretically [40,45,46] demonstrated that the two are the main factors for the surface reactivity of N-CNTs and they induce chemical activeness via different mechanisms. In comparison, the pyridine-like N configuration can induce a stronger binding energy to the adsorption of metal atoms [40,46]. In addition, it was also demonstrated that CN bonds are thermally stable [44,47,48] and the two primary configurations can stand an annealing of up to 800 °C [44].

Upon this point, it is clear that the initiation of ALD-SnO$_2$ was likely induced by the interaction of SnCl$_4$ with N-related defects and the two main doped-N configurations should be exempt from structural changes during ALD-SnO$_2$ as well, where growth temperatures of less than 400 °C were applied. In this case, it will be insightful to investigate the effects of N-doping by differentiating their configurations and changes. To fulfill this goal, we applied XPS to study three samples of N-CNTs grown on Si wafers. One control sample consists of pristine (uncoated) N-CNTs, and two comparative samples consist of N-CNTs coated with 100-cycle SnO$_2$ at 200 and 400 °C, respectively. Fig. 5 shows the XPS surveys of the three samples. The XPS spectrum of the uncoated N-CNTs (Fig. 5(a)) displays two characteristic peaks around 285 and 399 eV, corresponding to C 1s and N 1s, respectively. In addition, there are relatively weak peaks for O 1s, Fe 2p, and Si 2s as well, attributing to the Si wafer covered by a layer of native SiO$_2$ as well as a layer of iron catalyst. The XPS spectra for the two coated samples are shown in Fig. 5(b) and (c). In comparison, the N 1s peaks of the coated samples are significantly reduced while their C 1s peaks remain at a comparable level. Due to ALD-SnO$_2$, the coated samples show the newly appeared peaks of Sn and Cl, as well as some increase in the O 1s peaks. The weak Cl peaks are due to unreacted Cl ligands in ALD-SnO$_2$. In terms of a full width of at half-maximum (FWHM), it is found that the value for C 1s slightly decreases from 2.95 eV (Fig. 5(a)) to 2.87 eV (Fig. 5(b)) and 2.92 eV (Fig. 5(c)), while the value for N 1s significantly increases from
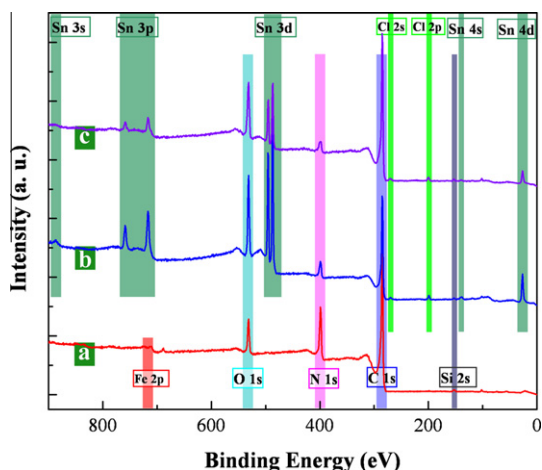
Fig. 5 – Survey scans of XPS spectra for (a) pristine N-CNTs, as well as N-CNTs coated with 100-cycle ALD-SnO$_2$ at (b) 200 °C and (c) 400 °C.

3.23 eV (Fig. 5(a)) to 3.86 eV (Fig. 5(b)) and 5.38 eV (Fig. 5(c)). As the indicators for the main compositions of N-CNTs, the narrowing C 1s and broadening N 1s peaks are essential for understanding the effects of N-doping and therefore deserve a further investigation with their high resolution spectra.

The high resolution C 1s spectra of the three samples are shown in Fig. 6(a)–(c), in which the dashed lines represent raw data and the solid lines are the corresponding fittings. The asymmetric C 1s spectra are commonly deconvoluted into five sub-peaks: PC1 (284.6 eV) [49] for the C–C bonds of graphite showing a peculiar dissymmetric shape, PC2–PC4 (285.5–289 eV) [50,51] for overlapping defective carbon structures due to C–N and C–O bonds, and π–π* transition (291 eV) [49], respectively. In comparison to the uncoated sample (Fig. 6(a)), it is observed that the defective sub-peaks (PC2–PC4) of the two coated samples (Fig. 6(b) and (c)) show some decrease. Quantitatively, the areal ratio between the areal addition of PC2–PC4 and the area of PC1 is 0.47, 0.34, and 0.29 for the uncoated sample and the two samples coated at 200 and 400 °C, respectively. The reducing areal ratio accounts for a decreasing area of the defective peaks and suggests that ALD-SnO$_2$ preferentially happened on the defective sites, for the deposited SnO$_2$ could lead to a block effect on XPS measurements of the defective sites. In a much clearer view, the three C 1s peaks are compared in the inset of Fig. 6(c). In comparison to the uncoated sample (marked as "a"), the C 1s peak for the sample coated at 200 °C (marked as "b") becomes narrower and weaker. This should be incurred by the uniform deposition of SnO$_2$ nanoparticles (as shown in Fig. 2(c) and (d)). On the other hand, the C 1s peak for the sample coated at 400 °C (marked as "c") only shows a slight decrease along the centered line while there is an evident reduction in the defective area. These changes are consistent with the selective deposition of SnO$_2$ nanoparticles at 400 °C (as shown in Fig. 3(b)), in which some defective sites must have been preferentially covered. Based on the above discussion, it is reasonable to conclude that N-related defective sites are responsible for the deposition of SnO$_2$.
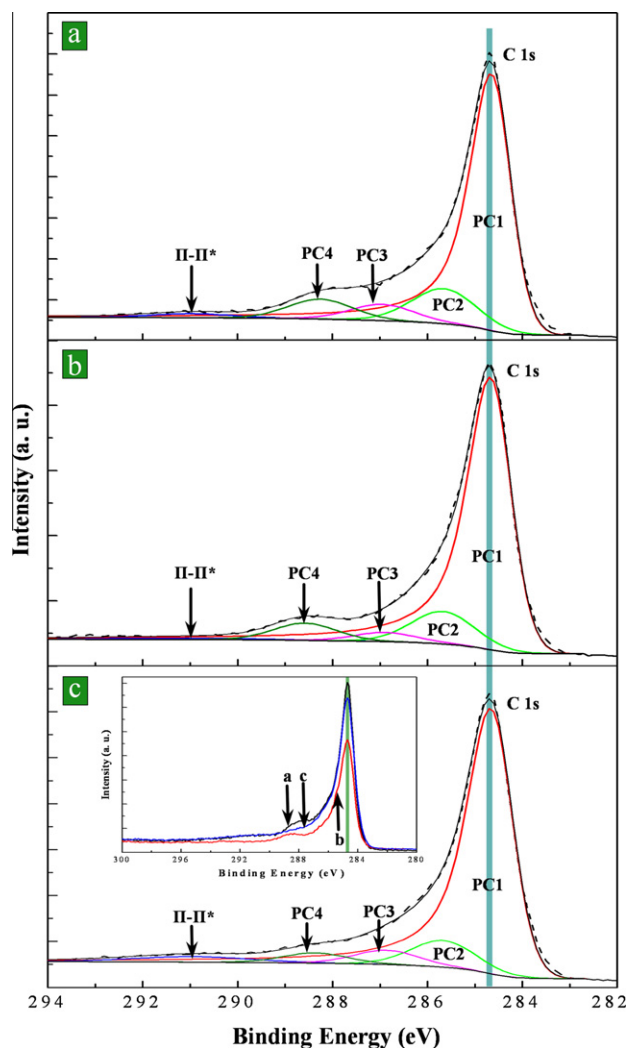
Fig. 6 – High-resolution XPS spectra of C 1s peak for (a) pristine N-CNTs as well as for N-CNTs coated with 100-cycle ALD-SnO$_2$ at (b) 200 °C and (c) 400 °C (inset: comparison of C 1s peaks).

To further clarify the roles of different doped-N configurations, Fig. 7(a)–(c) show the N 1s spectra of the three samples with high resolution, in which the dashed lines represent raw data and the solid lines are the corresponding fittings. The N 1s spectrum of the uncoated sample (Fig. 7(a), a N content of 14.8 at.%) was deconvoluted into four peaks: PN1 (398.7 eV) [44,52] ascribed to the pyridine-like N configuration, PN2 (400.8 eV) [44,52] corresponding to the graphite-like N configuration, as well as PN3 (403.5 eV) and PN4 (405.6 eV) [36] both attributing to nitrogen oxides. As for the two coated samples, it is observed from Fig. 7(b) and (c) that the PN1 peak reduces more evidently than PN2 peak in both cases. The areal ratio between PN1 and PN2 is 4.56, 2.27, and 2.00 for the uncoated sample and the two samples coated at 200 and 400 °C, respectively. The reducing areal ratio strongly suggests that SnO$_2$ were deposited on the defective sites of the two types but the deposition was more preferential for the pyridine-like N configuration. The selectiveness becomes stronger with growth temperature. In addition, it is also observed from
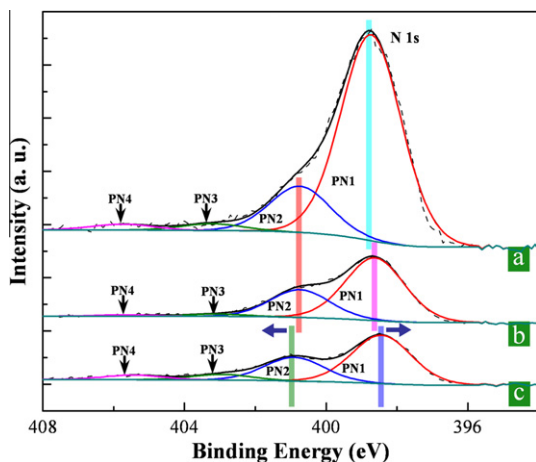
Fig. 7 – High-resolution XPS spectra of N 1s peak for (a) pristine N-CNTs as well as for N-CNTs coated with 100-cycle ALD-SnO₂ at (b) 200 °C and (c) 400 °C.

Fig. 7 that the PN1 centered lines of the coated samples move towards the low energy region (right-shifting), implying that the deposited SnO₂ chemically bonded to pyridine-like N configurations. In particular, the energy right-shifting is much larger with the sample coated with crystalline SnO₂ at 400 °C (Fig. 7(c)). On the other hand, it is also noted that there is a shift with the PN2 centered line of the sample coated at 400 °C (Fig. 7(c)), moving towards the high energy region (left-shifting). The energy left-shifting as well as the larger energy right-shifting with the sample coated at 400 °C suggests that crystalline SnO₂ must have induced stronger interactions to both the pyridine-like and graphite-like N configuration than those incurred by amorphous SnO₂ deposited at 200 °C. The opposite shifting of PN1 and PN2 is evidence to the previous claim [40,46]: pyridine-like and graphite-like N configuration take effect on deposition with different mechanisms. In pyridine-like N configurations, the N atoms could directly bond with metal atoms; in graphite-like N configurations, the N atoms could not bond with metal atoms directly but mediated their neighboring C atoms to bond with metal atoms [40,46]. It is also worth noting that for a given coated sample its pyridine-like N atoms shifted more in binding energy than its graphite-like N atoms. This is in well agreement with the earlier claim that the pyridine-like N configuration induces a stronger binding energy to metal atoms than the graphite-like N one. In addition, it needs to mention that nitrogen oxides (PN3 and PN4) are not counted as main factors in this discussion, due to their low compositions. If one would compare Fig. 7(c) with (a), it is not difficult to observe that nitrogen oxides have little change after ALD-SnO₂. The reduction of nitrogen oxides in Fig. 7(b) may be due to a full coverage of SnO₂ on N-CNTs (see Fig. 2(d)), which induced some block to XPS measurements.
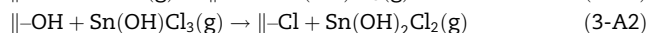
Based on the above discussion, it is reasonable to conclude that defective sites induced by N-doping are responsible for the initiation of ALD-SnO₂. Of the doped-N configurations, the pyridine-like and graphite-like ones are the main forces for ALD-SnO₂. In comparison, the pyridine-like N atoms took the predominant roles, for they provided higher binding energies to certain precursor atoms. This predominance became

more evident with an increased growth temperature, for the adsorption of atoms needs a higher binding energy under a higher temperature. As revealed in Fig. 3(f) and (g), there are more SnO₂ nanoparticles deposited in the regions of the interlinked nodes at 400 °C. These regions are dominated by the pyridine-like N configuration [53], and consequently higher binding energies provided by the pyridine-like N atoms led more SnO₂ nanoparticles to deposit in the interlinked nodes. Thus, this also explained why the coverage of SnO₂ decreased at 400 °C, in comparison to the cases at 200 and 300 °C.

3.2.2. The characteristics of surface chemistry

In addition to the above investigation on the effects of N-doping on ALD-SnO₂, we also explored the underlying mechanisms responsible for the growth characteristics of ALD-SnO₂. As revealed in Section 3.1, the ALD-SnO₂ showed a strong dependence on growth temperatures, resulting in amorphous nanoparticles/films (Fig. 2) at 200 °C, crystalline nanoparticles (Fig. 3) at 400 °C, and amorphous films embellished with crystalline nanoparticles (Fig. 4) at 300 °C. Obviously, there existed phase-transition in ALD-SnO₂ processes. To understand the temperature-dependent phase-transition, one view from surface chemistry will be helpful, for surface reactions are crucial and possible to change with temperature in ALD processes.

Earlier studies [54–56] noticed that the ALD processes of using metal chlorides and water as precursors always produced crystalline nanoparticles (e.g., TiO₂ or ZrO₂) on silica or alumina substrates when a threshold temperature (300 °C) was reached. Otherwise, amorphous films were formed at lower temperatures. More importantly, Puurunen [57] reviewed this sort of ALD processes, and further investigated the underlying mechanisms from a view of surface chemistry. It was suggested that the phase-transition of a deposited material is due to the changing ALD surface reactions with temperature, especially in the pulse of a metal chloride. This researcher postulated that ligand exchange (as described in Reaction (2-A)) dominates surface reactions at a growth temperature lower than 300 °C, while chlorination becomes predominant at a growth temperature higher than 300 °C. Ligand exchange competes against chlorination in ALD processes, and their dominance highly depends on the growth temperature. Based on Puurunen's work, we proposed both ligand exchange and chlorination for ALD-SnO₂ in this study. For a low growth temperature, the dominant ligand exchange happens in both the pulse of SnCl₄ and H₂O, as shown in Reactions (2-A) and (2-B), respectively. As a consequence, ligand exchange contributes to a layer-by-layer growth of SnO₂, as demonstrated in Fig. 2. For a high growth temperature, the dominant chlorination happens in the pulse of SnCl₄ as follows:

$$\|-OH + SnCl_4(g) \rightarrow \|-Cl + Sn(OH)Cl_3(g) \qquad (3\text{-}A1)$$
$$\|-OH + Sn(OH)Cl_3(g) \rightarrow \|-Cl + Sn(OH)_2Cl_2(g) \qquad (3\text{-}A2)$$

First, SnCl₄ chlorinates the surface hydroxyl groups and form an intermediate hydroxychloride molecule (Sn(OH)₂Cl₂) in a two-step reaction, as shown by Reactions (3-A1) and (3-A2). Then, the hydroxychlorides further react with surface chlorine groups via their hydroxyl groups, as shown in the following reaction:
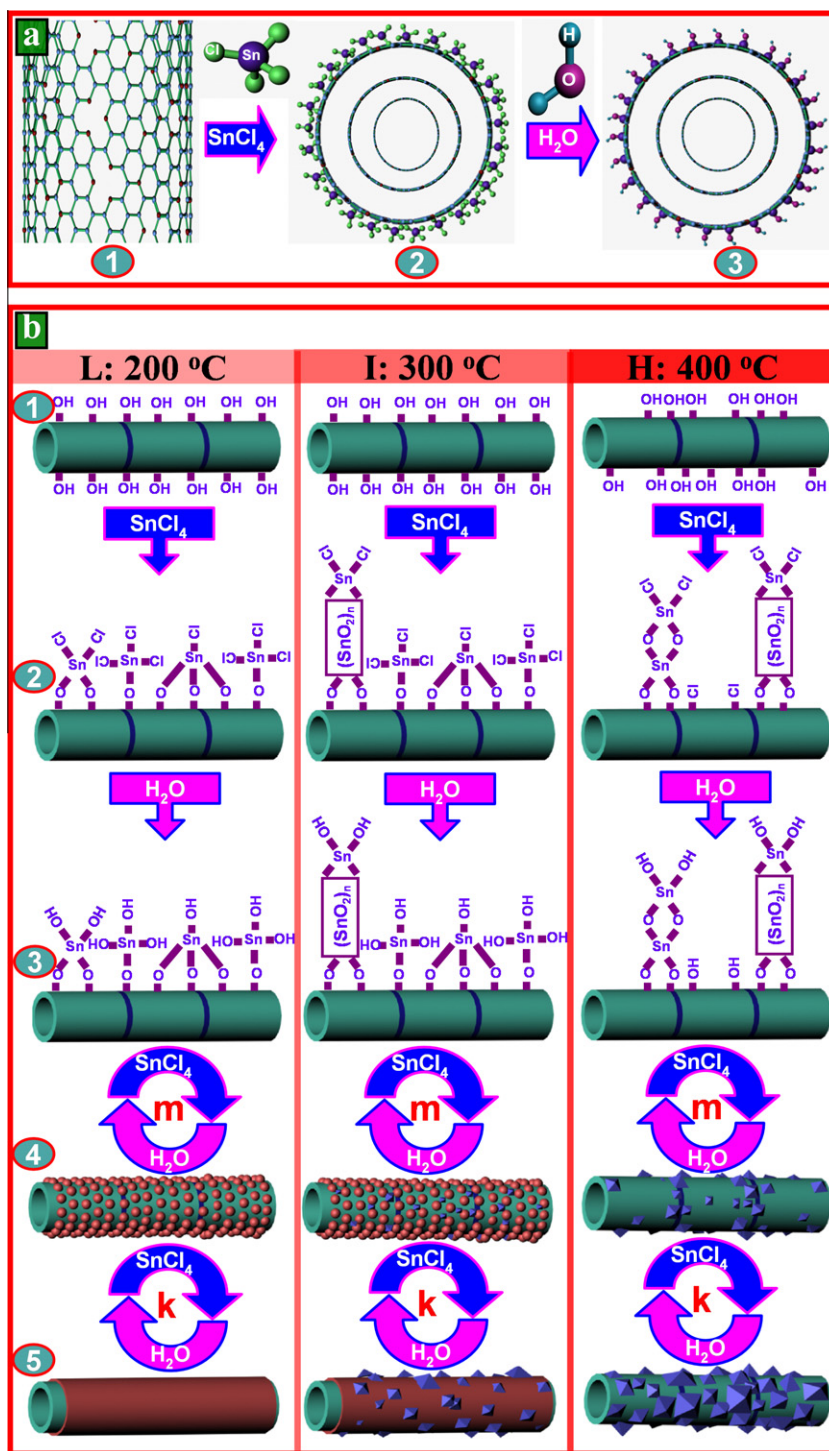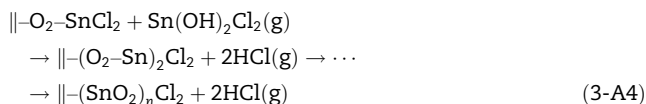
Fig. 8 – Schematic diagram of ALD-SnO$_2$ on N-CNTs. (a) The first ALD-SnO$_2$ cycle functionalized the surface of N-CNTs: (1) pristine N-CNTs decorated by N-doping defects, (2) SnCl$_4$ chemically adsorbed on N-CNTs in the first ALD half-reaction induced by N-doping defects, and (3) OH functional groups generated in the second ALD half-reaction induced by H$_2$O. (b) The temperature-dependent ALD-SnO$_2$ on N-CNTs: (1) N-CNTs (blue rings indicating interlinked nodes) uniformly covered by OH groups at low (L: 200 °C) and intermediate (I: 300 °C) temperature, but with more OH groups around interlinked nodes at high (H: 400 °C) temperature; (2) the half-reaction of SnCl$_4$ dominated by ligand exchange (L), chlorination (H), as well as a competition (I) between the two, respectively; (3) the half-reaction of H$_2$O dominated by ligand exchange in all the cases (L, I, and H); (4) N-CNTs deposited with tiny amorphous (L), crystalline (H), as well as coexisting amorphous-crystalline nanoparticles (I) after m-cycles ($m \leq 100$) of ALD-SnO$_2$; (5) N-CNTs deposited with coaxial amorphous film (L), coalesced crystalline nanoparticles (H), as well as coaxial amorphous film decorated with crystalline nanoparticles (I) after k-cycles ($k > 100$) of ALD-SnO$_2$.

$$2\|-Cl + Sn(OH)_2Cl_2(g) \rightarrow \|-O_2-SnCl_2 + 2HCl(g) \qquad (3-A3)$$
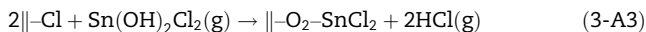
In particular, the chlorine groups on the right side of the above Reaction (3-A3) further react with hydroxychlorides in a chain of reactions, as shown in the following reaction:

$$\|-O_2-SnCl_2 + Sn(OH)_2Cl_2(g)$$
$$\rightarrow \|-(O_2-Sn)_2Cl_2 + 2HCl(g) \rightarrow \cdots$$
$$\rightarrow \|-(SnO_2)_nCl_2 + 2HCl(g) \qquad (3-A4)$$

As a consequence, a multilayer of SnO_2 is formed in one pulse of $SnCl_4$, accounting for a quicker growth of nanoparticles at a high temperature (e.g., 400 °C) than the one at a low temperature (e.g., 200 °C) after a same number of cycles. Additionally, it is worth noting that crystalline nanoparticles (shown in Figs. 3 and 4) varied in sizes, i.e., they did not nucleate at the same time and with a same rate. It is ascribed to the exposure variances of local sites in the pulse of $SnCl_4$. A sufficient exposure of $SnCl_4$ contributes to big nanoparticles grown on some sites while a deficient exposure of $SnCl_4$ leads to small nanoparticles grown on other sites. However, in a pulse of H_2O the surface reaction is the same as described in Reaction (2-B), and rewritten as:

$$\|-Cl + H_2O(g) \rightarrow \|-OH + HCl(g) \qquad (3-B)$$
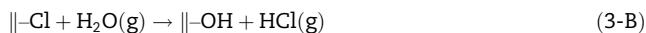
It is obvious that chlorination leads to a non-uniform growth of SnO_2, as demonstrated in Fig. 3. Furthermore, the case of ALD-SnO_2 at 300 °C (Fig. 4) provides a strong support to the competing behavior between ligand exchange and chlorination, resulting in amorphous films embellished with crystalline nanoparticles. Thus, it is reasonable to conclude that growth temperatures determined the phase-transition of SnO_2, at which different surface reactions are dominant. As for the limited coverage of SnO_2 at 400 °C, besides the reason due to the difference between different doped-N configurations (as discussed in Section 3.2.1), another reason is the deficient exposure of $SnCl_4$ to some local defective sites.

Furthermore, it is noteworthy that the ALD-SnO_2 at 200 °C experienced an island-like growth in the first 100 cycles before a layer of SnO_2 film was formed by the coalescence of nanoparticles. However, the island-like growth mode at 200 °C is different from the growth of crystalline nanoparticles at 400 °C in mechanism. The former one is determined by the reactive nature of the N-CNT surface (mainly due to density of functional groups) and presents a substrate-inhibited characteristic, while the latter one is mainly due to the chlorination as discussed above.

To further help form a better understanding on this study, we schematically summarized the characteristics of the ALD-SnO_2 on N-CNTs in Fig. 8. Fig. 8(a) emphasizes the effects of N-doping. Fig. 8(a1) shows two main doped-N (pyridine-like and graphite-like) configurations in pristine N-CNTs. In the first ALD cycle, $SnCl_4$ is chemically adsorbed on the surface of N-CNTs via N-related defects (Fig. 8(a2)), and then chlorine (Cl) groups are replaced by hydroxyl (OH) groups in the following reaction (Fig. 8(a3)). According to our findings in this study, growth temperature took important influences on ALD-SnO_2. As shown in Fig. 8(b), the influences of temperature are clarified. First, the coverage of OH groups on N-CNTs changes with temperature (Fig. 8(b1)): there are more OH groups around interlinked nodes (indicated by blue rings on N-CNTs)

at a high (H: 400 °C) temperature while the distribution of OH groups is uniform at a low (L) and an intermediate (I) temperature. In a following $SnCl_4$ pulse, the surface reactions are temperature-dependent. In Fig. 8(b2), ligand exchange (L column) and chlorination (H column) are dominant at a low and high temperature, respectively. For an intermediate temperature (I column), the two reactions compete and coexist with each other. In a following H_2O pulse (Fig. 8(b3)), however, ligand exchange is dominant for all the temperatures. Repeating ALD-SnO_2 with m-cycles (≤ 100) (Fig. 8(b4)), the deposited SnO_2 presents amorphous (L column), crystalline (H column), and coexisting amorphous-crystalline nanoparticles (I column) for different temperatures. In addition, the coverage is mainly dependent on the initial distribution of OH groups (Fig. 8(b1)). With increased k-cycles (>100) (Fig. 8(b5)), coaxial films are formed on N-CNTs at a low (L column) and an intermediate temperature (I column), but the latter is decorated with some growing crystalline nanoparticles. At a high temperature (H column), only crystalline nanoparticles are deposited and grow with a tendency to coalesce.

In summary, the ALD-SnO_2 on N-CNTs is temperature-dependent via two routes: (i) the adsorption of the tin source precursor ($SnCl_4$) on the surface of N-CNTs was reduced with a increased growth temperature, owing to the variances of different doped-N configurations to chemically adsorb precursor molecules; (ii) the inherent surface reactions changed with growth temperature and there was a competition between ligand exchange and chlorination for dominance. Consequently, the synthesized hybrid nanostructures present controllable phases: amorphous (dominated by ligand exchange), crystalline (dominated by chlorination), as well as a coexisting amorphous-crystalline phase (dominated by the competition between ligand exchange and chlorination). In addition, the morphologies of the deposited SnO_2 are also controllable, presenting coaxial nanoparticles or nanofilms.

4. Conclusions

In this paper, we demonstrated a strategy to synthesize a series of novel SnO_2-CNT hybrid materials in a highly controllable means. This strategy was featured by applying ALD-SnO_2 directly on N-CNTs and exhibited some unique advantages. First of all, the N-CNTs could initiate the following ALD-SnO_2 directly, exempt from any pretreatment as widely used for undoped CNTs. In addition, ALD benefited the deposited SnO_2 with tunable morphologies from nanoparticles to nanofilms. Furthermore, the temperature-dependent nature of surface reactions contributed the deposited SnO_2 to controllable phases from amorphous to crystalline or a coexisting amorphous-crystalline phase. In order to get a better understanding on the role of N-CNTs and the temperature-dependent nature of ALD-SnO_2, we also explored the underlying mechanisms. Using XPS, we first investigated the effects of N-doping on the initiation of ALD-SnO_2. It was revealed that N-related defects were crucial, especially the graphite-like and pyridine-like N configuration. In comparison, pyridine-like N configuration played a more important role in ALD-SnO_2. As for the controllable phases with growth temperature, it was suggested that different growth temperatures induced different surface reactions in ALD-SnO_2 and thereby

determined the phase of the deposited SnO_2. It is believed that ligand exchange was dominant at low temperatures while chlorination was paramount at high temperatures. The former led to amorphous SnO_2 deposited at 200 °C while the latter was responsible for crystalline SnO_2 deposited at 400 °C. The two competed with each other with temperature, and led to a coexisting amorphous-crystalline phase of SnO_2 deposited at 300 °C. As a consequence, this work not only fulfilled a new strategy for synthesizing SnO_2-CNT hybrid materials but provided the underlying mechanisms for a better understanding as well. In particular, these novel SnO_2-CNT hybrids have great potential applications in many important areas, such as lithium-ion batteries, and gas-sensors.

Acknowledgements

REFERENCES

[1] Monthioux M, Kuznetsov VL. Who should be given the credit for the discovery of carbon nanotubes. Carbon 2006;44(9):1621–3.

[2] Iijima S. Helical microtubules of graphitic carbon. Nature 1991;354(6348):56–8.

[3] Dai H. Carbon nanotubes: synthesis, integration, and properties. Acc Chem Res 2002;35(12):1035–44.

[4] Zhang H, Cao G, Yang Y. Carbon nanotube arrays and their composites for electrochemical capacitors and lithium-ion batteries. Energy Environ Sci 2009;2(9):932–43.

[5] Li Z, Wang H, Liu P, Zhao B, Zhang Y. Synthesis and field-emission of aligned SnO_2 nanotubes arrays. Appl Surf Sci 2009;255(8):4470–3.

[6] Ma LA, Guo TL. Synthesis and field emission properties of needle-shaped SnO_2 nanostructures with rectangular cross-section. Mater Lett 2009;63(2):295–7.

[7] Batzill M. Surface science studies of gas sensing materials: SnO_2. Sensors 2006;6(10):1345–66.

[8] Idota Y, Kubota T, Matsufuji A, Maekawa Y, Miyasaka T. Tin-based amorphous oxide: a high-capacity lithium-ion-storage material. Science 1997;276(5317):1395–7.

[9] Zhao N, Fu L, Yang L, Zhang T, Wang G, Wu Y, et al. Nanostructured anode materials for Li-ion batteries. Pure Appl Chem 2008;80(11):2283–95.

[10] Cheng F, Tao Z, Liang J, Chen J. Template-directed materials for rechargeable lithium-ion batteries. Chem Mater 2008;20(3):667–81.

[11] Yang A, Tao X, Wang R, Lee S, Surya C. Room temperature gas sensing properties of SnO_2/multiwall-carbon-nanotube composite nanofibers. Appl Phys Lett 2007;91(13):133110–3.

[12] Gong J, Sun J, Chen Q. Micromachined sol–gel carbon nanotube/SnO_2 nanocomposite hydrogen sensor. Sens Actuators B 2008;130(2):829–35.

[13] Hoa ND, Quy NV, Song H, Kang Y, Cho Y, Kim D. Tin oxide nanotube structures synthesized on a template of single-walled carbon nanotubes. J Cryst Growth 2009;311(3):657–61.

[14] Kuang Q, Li SF, Xie ZX, Lin SC, Zhang XH, Xie SY, et al. Controllable fabrication of SnO_2-coated multiwalled carbon nanotubes by chemical vapour deposition. Carbon 2006;44(7):1166–72.

[15] Han WQ, Zettl A. Coating single-walled carbon nanotubes with tin oxide. Nano Lett 2003;3(5):681–3.

[16] Wen Z, Wang Q, Zhang Q, Li J. In situ growth of mesoporous SnO_2 on multiwalled carbon nanotubes: a novel composite with porous-tube structure as anode for lithium batteries. Adv Funct Mater 2007;17(15):2772–8.

[17] Zhang HX, Feng C, Zhai YC, Jiang KL, Li QQ, Fan SS. Cross-stacked carbon nanotube sheets uniformly loaded with SnO_2 nanoparticles: a novel binder-free and high-capacity anode material for lithium-ion batteries. Adv Mater 2009;21(22):2299–304.

[18] Myung Y, Jang DM, Cho YJ, Kim HS, Park J, Kim JU, et al. Nonenzymatic amperometric glucose sensing of platinum, copper sulphide, and tin oxide nanoparticle–carbon nanotube hybride nanostructures. J Phys Chem C 2009;113(4):1251–9.

[19] Chen G, Wang Z, Xia D. One-pot synthesis of carbon nanotube@SnO_2–Au coaxial nanocable for lithium-ion batteries with high-rate capability. Chem Mater 2008;20(22):6951–6.

[20] Du N, Zhang H, Chen B, Ma X, Huang X, Tu J, et al. Synthesis of polycrystalline SnO_2 nanotubes on carbon nanotube template for anode material of lithium-ion battery. Mater Res Bull 2009;44(1):211–5.

[21] Terrones M, Jorio A, Endo M, Rao AM, Kim YA, Hayashi T, et al. New direction in nanotube science. Mater Today 2004;7(10):30–45.

[22] George SM. Atomic layer deposition: an overview. Chem Rev 2010;110(1):111–31.

[23] Knez M, Nielsch K, Niinistö L. Synthesis and surface engineering of complex nanostructures by atomic layer deposition. Adv Mater 2007;19(21):3425–38.

[24] Kim H, Lee HBR, Maeng WJ. Applications of atomic layer deposition to nanofabrication and emerging nanodevices. Thin Solid Films 2008;517(8):2563–80.

[25] Rosental A, Tarre A, Gerst A, Uustare T, Sammelselg V. Atomic-layer chemical vapor deposition of SnO_2 for gas-sensing applications. Sens Actuators B 2001;77(1–2):297–300.

[26] Tarre A, Rosental A, Sammelselg V, Uustare T. Comparative study of low-temperature chloride atomic-layer chemical vapor deposition of TiO_2 and SnO_2. Appl Surf Sci 2001;175:111–6.

[27] Tarre A, Rosental A, Aidla A, Aarik J, Sundqvist J, Hårsta A. New routes to SnO_2 heteroepitaxy. Vacuum 2002;67(3–4):571–5.

[28] Takeuchi T, Shoji K, Tadano T, Doteshita I, Onodera S. Preparation of sub-nanometer thickness-controlled thin dioxide films by pulsed atomic-layer CVD. Thin Solid Films 2003;442(1–2):98–101.

[29] Rosental A, Tarre A, Gerst A, Sundqvist J, Hårsta A, Aidla A, et al. Gas sensing properties of epitaxial SnO_2 thin films prepared by atomic layer deposition. Sens Actuators B 2003;93(1–3):552–5.

[30] Takeuchi T, Doteshita I, Asami S. Epitaxial growth of sub-nanometre thick thin dioxide films on sapphire substrates by pulsed atomic layer chemical vapour deposition. Surf Interf Anal 2004;36(8):1133–5.

[31] Lu J, Sundqvist J, Ottosson M, Tarre A, Rosental A, Aarik J, et al. Microstructure characterisation of ALD-grown epitaxial SnO_2 thin films. J Cryst Growth 2004;260(1–2):191–200.

[32] Natarajan G, Cameron DC. Influence of oxygen depletion layer on the properties of tin oxide gas-sensing films fabricated by atomic layer deposition. Appl Phys A 2009;95(3):621–7.

[33] Du X, Du Y, George SM. In situ examination of tin oxide atomic layer deposition using quartz crystal microbalance and Fourier transform infrared techniques. J Vac Sci Technol A 2005;23(4):581–8.

[34] Ferguson JD, Buechler KJ, Weimer AW, George SM. SnO$_2$ atomic layer deposition on ZrO$_2$ and Al nanoparticles: pathway to enhanced thermite materials. Powder Technol 2005;156(2–3):154–63.

[35] Du X, Du Y, George SM. CO gas sensing by ultrathin tin oxide films grown by atomic layer deposition using transmission FTIR spectroscopy. J Phys Chem A 2008;112(39):9211–9.

[36] Zhong Y, Jaidann M, Zhang Y, Zhang G, Liu H, Ionescua MI, et al. Synthesis of high nitrogen doping of carbon nanotubes and modeling the stabilization of filled DAATO@CNTs (10, 10) for nanoenergetic materials. J Phys Chem Solids 2010;71(2):134–9.

[37] Puurunen RL. Surface chemistry of atomic layer deposition: a case study for the trimethylaluminum/water process. J Appl Phys 2005;97(12):121301–52.

[38] Peng S, Cho K. Ab inito study of doped carbon nanotube sensors. Nano Lett 2003;3(4):513–7.

[39] Sun CL, Chen LC, Su MC, Hong LS, Chyan O, Hsu CY, et al. Ultrafine platinum nanoparticles uniformly dispersed on arrayed CNx nanotubes with high electrochemical activity. Chem Mater 2005;17(14):3749–53.

[40] Yang SH, Shin WH, Lee JW, Kim HS, Kang JK, Kim YK. Nitrogen-mediated fabrication of transition metal-carbon nanotube hybrid materials. Appl Phys Lett 2007;90(1). 013103–3.

[41] Sun S, Zhang G, Zhong Y, Liu H, Li R, Zhou X, et al. Ultrathin single crystal Pt nanowires grown on N-doped carbon nanotubes. Chem Commun 2009;45:7048–50.

[42] Choi HC, Park J, Kim B. Distribution and structure of N atoms in multiwalled carbon nanotubes using variable-energy X-ray photoelectron spectroscopy. J Phys Chem B 2005;109(10):4333–40.

[43] Yang SH, Shin WH, Kang JK. The nature of graphite- and pyridine-like nitrogen configurations in carbon nitride nanotubes: dependence on diameter and helicity. Small 2008;4(4):437–41.

[44] Choi HC, Bae SY, Jang WS, Park J, Song HJ, Shin HJ, et al. Release of N$_2$ from the carbon nanotubes via high-temperature annealing. J Phys Chem B 2005;109(5):1683–8.

[45] Stafström S. Reactivity of curved and planar carbon–nitride structures. Appl Phys Lett 2000;77(24):3941–3.

[46] Li YH, Hung TH, Chen CW. A first-principles study of nitrogen- and boron-assisted platinum adsorption on carbon nanotubes. Carbon 2009;47(3):850–5.

[47] Li JJ, Zheng WT, Wu HH, Sun L, Gu GG, Bian HJ, et al. Compositional and structural modifications of amorphous carbon nitride films induced by thermal annealing. J Phys D: Appl Phys 2003;36(16):2001–5.

[48] Li JJ, Zheng WT, Jin ZS, Gai TX, Gu GR, Bian HJ, et al. Thermal stability of magnetron sputtering amorphous carbon nitride films. Vacuum 2004;72(3):233–9.

[49] Estrade-Szwarckopf H. XPS photoemission in carbonaceous materials: a "defect" peak beside the graphitic asymmetric peak. Carbon 2004;42(8–9):1713–21.

[50] Marton D, Boyd KJ, Al-Bayati AH, Todorov SS, Rabalais JW. Carbon nitride deposited using energetic species: a two-phase system. Phys Rev Lett 1994;73(1):118–21.

[51] Chan LH, Hong KH, Xiao DQ, Lin TC, Lai SH, Hsieh WJ, et al. Resolution of the binding configuration in nitrogen-doped carbon nanotubes. Phys Rev B 2004;70(12). 125408–7.

[52] Maldonado S, Morin S, Stevenson KJ. Structure, composition, and chemical reactivity of carbon nanotubes by selective nitrogen doping. Carbon 2006;44(8):1429–37.

[53] Terrones M, Ajayan PM, Banhart F, Blase X, Carroll DL, Charlier JC, et al. N-doping and coalescence of carbon nanotubes: synthesis and electronic properties. Appl Phys A 2002;74(3):355–61.

[54] Haukka S, Lakomaa EL, Root A. An IR and NMR study of the chemisorption of TiCl$_4$ on silica. J Phys Chem 1993;97(19):5085–94.

[55] Haukka S, Lakomaa EL, Jylhä O, Vilhunen J, Hornytzkyj S. Dispersion and distribution of titanium species bound to silica from TiCl$_4$. Langmuir 1993;9(12):3497–506.

[56] Kytökivi A, Lakomaa EL, Root A. Controlled formation of ZrO$_2$ in the reaction of ZrCl$_4$ vapor with porous silica and γ-alumina surfaces. Langmuir 1996;12(18):4395–403.

[57] Puurunen RL. Formation of metal oxide particles in atomic layer deposition during the chemisorption of metal chlorides: a review. Chem Vapor Depos 2005;11(2):79–90.